Brazilian Journal of Physics (2023) 53:96
https://doi.org/10.1007/s13538-023-01302-z

GENERAL AND APPLIED PHYSICS

E × B Drift Particle Transport in Tokamaks

L.A. Osorio-Quiroga[1] · G.C. Grime[1] · M. Roberto[2] · R.L. Viana[1,3] · Y. Elskens[4] · I.L. Caldas[1]

Received: 24 March 2023 / Accepted: 14 April 2023 / Published online: 23 May 2023

Abstract
In tokamaks, modification of the plasma profiles can reduce plasma transport, improving particle confinement. However, this improvement is still not completely understood. In this work, we consider a drift wave test particle model to investigate the influence of the electric and magnetic field profiles on plasma transport. Test particle orbits subjected to $\mathbf{E} \times \mathbf{B}$ drift are numerically integrated and their transport coefficient is obtained. We conclude that sheared profiles reduce particle transport, even for high amplitude perturbations. In particular, nonmonotonic electric and magnetic fields produce shearless transport barriers, which are particularly resistant to perturbations and reduce even more the transport coefficient.

Keywords Tokamak · Shearless transport barrier · $\mathbf{E} \times \mathbf{B}$ drift · Transport coefficient

1 Introduction

Tokamaks are one of the most promising devices for achieving commercial thermonuclear fusion power [1]. However, particle transport limits the plasma confinement. For instance, electrostatic instabilities at the plasma edge produce turbulences leading to an $\mathbf{E} \times \mathbf{B}$ drift in the particle motion, producing the so-called anomalous transport [2].

For some enhanced scenarios of tokamak discharges, the plasma has regions with reduced transport coefficients, known as plasma transport barriers [3]. Some advances in the understanding of the relation between plasma profiles and the presence of transport barriers were achieved in [4]. A transport reduction has been considered due to the $\mathbf{E} \times \mathbf{B}$ shear caused by the electric field profile [5–7]. However, these models treat turbulent transport and fluctuation amplitude as a single fluctuating quantity [8].

Another approach to describe the onset and destruction of plasma transport barriers regards not only the shear of plasma profiles but also its curvature [9]. Recently, experimental evidence pointed out that, for some regimes, the curvature effects suppress the transport, and this suppression is independent of fluctuations amplitude [10]. In this context, models in which the suppression transport is decorrelated from the amplitude of the fluctuations are needed. One of them is based on shearless transport barriers [11].

The shearless transport barriers appear in tokamak plasmas with nonmonotonic electric or magnetic field radial profiles [12, 13]. In fact, the location of these transport barriers is associated with the radial position where the plasma profile shear is null, and it is related to nontwist phenomena in Hamiltonian systems [14–17].

A plasma model to investigate the transport reduction at the plasma edge was proposed by Horton et al. [18]. This model uses area-preserving maps to describe the motion of test particles subject to the electrostatic drift waves. In this model, particle transport is caused by chaotic orbits that arise in the phase space by the effect of drift wave oscillations.

Some works have considered the influence of the plasma profiles on particle transport regarding Horton's model. Inserting nonmonotonic profiles, nontwist phenomena appear, i.e., a shearless curve acts as a robust barrier preventing the chaotic orbits from escaping the plasma. This

Dedicated to Professor Silvio R. A. Salinas on the occasion of his 80th birthday.

✉ G.C. Grime
gabrielgrime@gmail.com

[1] Institute of Physics, University of São Paulo, São Paulo 05508-090, São Paulo, Brazil

[2] Physics Department, Aeronautics Institute of Technology, São José dos Campos 12228-900, São Paulo, Brazil

[3] Physics Department, Federal University of Paraná, Curitiba 81531-990, Paraná, Brazil

[4] Aix-Marseille Université , UMR 7345 CNRS, PIIM, Marseille 13397, France

nonmonotonicity can be related to the electric [19–21] or magnetic field profiles [22, 23].

In this work, we study the influence of such nonmonotonic profiles on plasma transport using Horton's model. The numerical computations indicate the absence of a shearless transport barrier when monotonic profiles are applied. When a nonmonotonic radial electric field profile is used, the shearless curve appears. In addition, this shearless curve can be destroyed by varying the fluctuation amplitudes, or by modifying the electric and magnetic field profiles. Furthermore, we varied the amplitude of the perturbing modes and obtained the transport coefficient associated with some scenarios of plasma profiles. The results indicate a reduction of the transport in sheared and, especially, in reversed shear scenarios.

The paper is organized as follows. Section 2 is devoted to presenting the particle transport drift wave model used in this work. In Sect. 3 we present the influence of the radial electric and magnetic field profiles in the onset and breakup of shearless transport barriers. In Sect. 4 we show the transport coefficient analysis. Conclusions are in Sect. 5.

2 Drift-Wave Transport Model

Plasmas are composed of electrons and ions that move by the effect of electromagnetic fields. A test particle in the plasma moves subject to an electric field $\mathbf{E}$ and a magnetic field $\mathbf{B}$, whose cross product $\mathbf{E}\times\mathbf{B}$ produces an important drift that causes radial transport at the plasma edge in tokamaks [2, 24].

Horton's model was proposed to investigate the origins of the transport reduction in reversed shear electric and magnetic field profiles [18]. It is based on the motion of a test particle in the plasma, whose guiding-center moves according to the equation

$$\dot{\mathbf{x}} = v_{\parallel}\hat{b} + \mathbf{v}_{\mathbf{E}\times\mathbf{B}}, \quad \mathbf{v}_{\mathbf{E}\times\mathbf{B}} = \frac{\mathbf{E}\times\mathbf{B}}{B^2}, \tag{1}$$

which has two components: a velocity in the direction of the magnetic field, $\hat{b} = \mathbf{B}/B$, and a drift caused by the cross product $\mathbf{v}_{\mathbf{E}\times\mathbf{B}}$. The dot notation is reserved for total time derivatives, like $\dot{\mathbf{x}} = \mathrm{d}\mathbf{x}/\mathrm{d}t$. In order to study anomalous transport, other drifts, such as the curvature and gradient of the magnetic field, can be neglected because they have length and time scales larger than the $\mathbf{E}\times\mathbf{B}$ drift. In this limit, the tokamak has a large aspect ratio, i.e., $\epsilon = a/R \ll 1$, where a and R are the minor and major radius of the plasma, as illustrated in Fig. 1.

The system of Eq. (1) is rewritten into components using pseudo-toroidal coordinates, where $\mathbf{x} = (r, \theta, \varphi)$ is the position vector, r the radial component, φ and θ the toroidal and poloidal angles, respectively, Fig. 1.

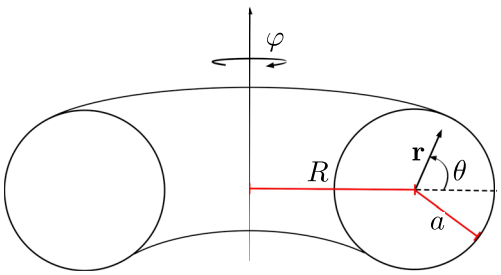

Fig. 1 Representation of the tokamak plasma in pseudo-toroidal coordinates, where R is the major axis and a is the minor axis of the plasma. The pseudo-toroidal coordinates consist of the toroidal angle φ, polar angle θ and radial distance r

The electric field considered is the sum of an equilibrium and a fluctuating part, such that

$$\mathbf{E}(\mathbf{x}, t) = \mathbf{E}_r(r)\hat{r} + \tilde{\mathbf{E}}(\mathbf{x}, t). \tag{2}$$

The fluctuating electric field $\tilde{\mathbf{E}}$ characterizes the electrostatic fluctuations at the plasma edge, originating the anomalous transport. Due to its electrostatic nature, $\nabla\times\tilde{\mathbf{E}} = 0$, the fluctuating electric field can be written as the gradient of an electrostatic potential $\tilde{\phi}$, such that, $\tilde{\mathbf{E}} = -\nabla\tilde{\phi}$. Horton's model establishes this potential as a Fourier expansion

$$\tilde{\phi}(\theta, \varphi, t) = \sum_n \phi_n \cos\left(M\theta - L\varphi - n\omega_0 t - \alpha_n\right), \tag{3}$$

where M and L are the dominant spatial modes of the fluctuation, ω_0 its fundamental angular frequency, ϕ_n and α_n the amplitude and phase of the harmonics, respectively. In general, the electrostatic fluctuations amplitude has a radial dependence; however, for the purpose of this work, it is considered constant [25].

We consider a plasma equilibrium configuration with the magnetic field given by

$$\mathbf{B}(r) = B_\theta(r)\hat{\theta} + B_\varphi\hat{\varphi}. \tag{4}$$

Since $B_\theta \sim \epsilon B_\varphi$, and $\epsilon \ll 1$ for large aspect-ratio tokamaks, we approximate $B \approx B_\varphi \gg B_\theta$. In this limit, the decomposition of Eq. (1) into components yields

$$\dot{r} = \frac{1}{Br}\frac{\partial\tilde{\phi}(\theta, \varphi, t)}{\partial\theta}, \tag{5a}$$

$$r\dot{\theta} = \frac{rv_{\parallel}(r)}{Rq(r)} - \frac{E_r(r)}{B}, \tag{5b}$$

$$R\dot{\varphi} = v_{\parallel}(r), \tag{5c}$$

where

$$q(r) = \frac{rB_\varphi}{RB_\theta(r)} \tag{6}$$

is the safety factor profile, another form of writing the radial dependence of the magnetic field.

Introducing the action-like $I = (r/a)^2$ and the angle-like $\psi = M\theta - L\varphi$ variables, and performing the adimentionalization presented in the Appendix, the equations of motion (5a–5c) reduce to the equations

$$\dot{I} = 2M \sum_n \phi_n \sin(\psi - n\omega_0 t - \alpha_n), \tag{7a}$$

$$\dot{\psi} = \epsilon v_\parallel \frac{M - Lq(I)}{q(I)} - \frac{M}{\sqrt{I}} E_r(I), \tag{7b}$$

which form a canonical pair of variables since they satisfy the condition

$$\frac{\partial \dot{\psi}}{\partial \psi} + \frac{\partial \dot{I}}{\partial I} = 0, \tag{8}$$

which implies the existence of a Hamiltonian function H such that

$$\frac{\mathrm{d}I}{\mathrm{d}t} = -\frac{\partial H}{\partial \psi}, \quad \frac{\mathrm{d}\psi}{\mathrm{d}t} = \frac{\partial H}{\partial I}. \tag{9}$$

Setting

$$\omega(I) = \epsilon v_\parallel \frac{[M - Lq(I)]}{q(I)} - \frac{M}{\sqrt{I}} E_r(I), \tag{10}$$

one can write the Hamiltonian as

$$H(I, \psi, t) = H_0(I) + H_1(\psi, t), \tag{11}$$

where

$$H_0(I) = \int^I \omega(I')\,\mathrm{d}I' \tag{12a}$$

$$H_1(\psi, t) = 2M\tilde{\phi} \tag{12b}$$

are the integrable and perturbative parts of the Hamiltonian system.

If $\phi_n = 0$ for all modes, I will be a constant of motion and the system will be integrable [26]. Here, the perturbative part H_1 will be zero and the dynamics of the system will be given by the integrable Hamiltonian $H_0(I)$. In this limit,

$$\dot{\psi}/\omega_0 = \omega(I)/\omega_0 = \nu(I) \tag{13}$$

gives the dimensionless frequency profile of the orbits. Orbits with rational frequency will have a periodic behavior, whereas orbits with irrational frequency, a quasiperiodic one; the latter ones form invariant curves in phase space.

For the perturbed Hamiltonian, $\phi_n \neq 0$, we have a fluctuating electric field component on the poloidal direction which results in the radial drift $\tilde{\mathbf{E}}_\theta \times \mathbf{B}_\varphi$. By the Poincaré-Birkhoff theorem, the rational-frequency orbits form islands [26]. Chaotic orbits also appear in phase space and they are bounded by the invariant curves.

After the last invariant curve breaks up, the chaotic trajectories occupy all the accessible phase space and global transport takes place. Moreover, breakup depends on whether the frequency profile has degeneracies, or not.

According to the KAM theorem, invariant curves whose frequency converges fast to rationals are easier to be destroyed [27], so, in systems that satisfy the twist condition, i.e.,

$$\left|\frac{\partial \omega(I)}{\partial I}\right| = \left|\frac{\partial^2 H_0}{\partial I^2}\right| > 0, \tag{14}$$

the last invariant curve to be broken up has a frequency value given by the golden mean [28]. On the other hand, in systems that do not satisfy the twist condition (14), called nontwist systems, invariant curves, which are particularly resistant to periodic perturbations, can appear where KAM theorem does not apply [29]; these curves are usually called shearless. Even when the shearless curve is broken up, a partial transport barrier still persists [30]. Hence, the nontwist systems have the so-called shearless transport barriers [17].

The model proposed by Horton was introduced to analyze the effects of reversed shear profiles of the electric and magnetic fields in plasma [18]. In this context, the introduction of nonmonotonic profiles of $E_r(I)$ and $q(I)$ yields a frequency profile $\omega(I)$ that violates the twist condition (14), resulting in the presence of shearless transport barriers in phase space.

In the next sections, we will show the effects of applying monotonic and nonmonotonic profiles in the Hamiltonian system (7a–7b). Mainly, we analyze the onset and breakup of shearless transport curves and the transport in phase space. For monotonic profiles, the system satisfies the twist condition. In addition, using a nonmonotonic profile of the electric field, a shearless transport barrier can emerge in phase space and prevent the transport of particles at the plasma edge. The variations of the plasma profiles can cause the breakup of this shearless curve.

3 Influence of the Plasma Profiles

The Hamiltonian system (7a–7b) has one degree of freedom and explicit time dependence with a characteristic angular frequency ω_0. Such time-periodic forced systems are commonly analyzed by a stroboscopic Poincaré section. We

numerically integrate the Eqs. (7a–7b) and plot the solutions at times $t_j = 2\pi j/\omega_0$, for $j = 0, 1, 2, \ldots, N$. So, given an initial condition $\mathbf{P}_0 = (\psi_0, I_0)$, we obtain the next point on the stroboscopic map, $\mathbf{P}_1 = (\psi_1, I_1)$, and all the subsequent ones until having the orbit $\Sigma = (\mathbf{P}_0, \mathbf{P}_1, \mathbf{P}_2, \ldots, \mathbf{P}_N)$. In this work, we applied the Dorman-Prince numerical integrator [31], with tolerance 10^{-13} and maximum stepsize 10^{-2}.

The results in this section and in Sect. 4 are based on parameters and plasma profiles from the TCABR tokamak [32]. However, the main conclusions can be generalized to other similar devices. For TCABR tokamak, the minor and major plasma radii are $a = 0.18$ m and $R = 0.61$ m, respectively, whereas the minor radius of the vessel chamber is $b = 0.21$ m. The toroidal magnetic field at the plasma center is $B = 1.2$ T, the inverse aspect ratio is $\epsilon \approx 0.3$, and the characteristic value of the electric field is regarded as $E_0 = 2.274$ kV/m. The floating potential parameters are taken based on experimental measurements [33], where for the dominant spatial modes we take $L = 4$ and $M = 16$, and 60 rad/ms for the fundamental angular frequency, which corresponds to $\omega_0 = 5.7$, after carrying out the normalization presented in the Appendix. We consider the phase $\alpha_n = \pi$ for all modes.

We are exploring the influence of reversed shear radial profiles of the electric and magnetic fields in plasma transport. Therefore, to avoid introducing the influence of the velocity profile effect, which can affect the twist condition, we assume that the guiding-center of the test particle moves along the magnetic field lines with a constant velocity of 3.79 km/s, which is consistent with experimental measurements [34] and corresponds to $v_{\parallel} = 2.00$, according to the normalization.

3.1 Radial Electric Field

The considered magnetic field is described by a monotonic safety factor profile given by

$$q(r) = \begin{cases} q_0 + \zeta\left(\frac{r}{a}\right)^2 & \text{if } r \le a, \\ q_a\left(\frac{r}{a}\right)^2 & \text{if } r > a, \end{cases} \tag{15}$$

where q_0 and q_a represent the values at the center and edge of the plasma, and in this case, they are 1.00 and 3.65, respectively. The value of ζ is equal to $q_a - q_0$.

To investigate the influence of the radial equilibrium electric field on plasma transport, we consider: (i) monotonic and (ii) nonmonotonic electric field radial profiles. In both scenarios, we use the same expression for the radial electric field [19], but we adjust the parameters to create different profiles. Specifically, we investigate a constant, a linear, and a parabolic profiles.

Then, let us consider the radial electric field profile as the one given by

$$E_r(r) = 3\alpha\left(\frac{r}{a}\right)^2 + 2\beta\left(\frac{r}{a}\right) + \gamma, \tag{16}$$

where α, β, and γ are control parameters that we can adjust.

3.1.1 Monotonic Electric Field

We consider a constant electric field profile for which $\alpha = \beta = 0$ and $\gamma = -0.77$, and a linear one for which $\alpha = 0$, $\beta = 0.79$ and $\gamma = -2.64$. We impose both electric fields to be equal at $I = 1.4$, a little further than the vessel wall, located at $I_{\text{wall}} = 1.36$.

In Fig. 2, we show the monotonic plasma profiles we are considering, the electric field and the safety factor. Furthermore, we show the shear of the electric field

$$S_{E_r}(r) = \frac{a}{E_r(r)}\frac{\mathrm{d}E_r(r)}{\mathrm{d}r}, \tag{17}$$

and the frequency profile, $\nu(I)$, obtained from Eq. (13). We emphasize that the frequency profile depends on the electric and magnetic field profiles. Changes in these profiles modify the frequency of the orbits and, consequently, the phase space configuration.

For the constant E_r, besides a null shear of the electric field, for the unperturbed Hamiltonian, the frequency profile obeys a monotonic behavior, satisfying the twist condition, Fig. 2(d). For this former scenario, we do not expect the appearance of any shearless curve. The same behavior is found for the linear electric field case: although the S_{Er} is

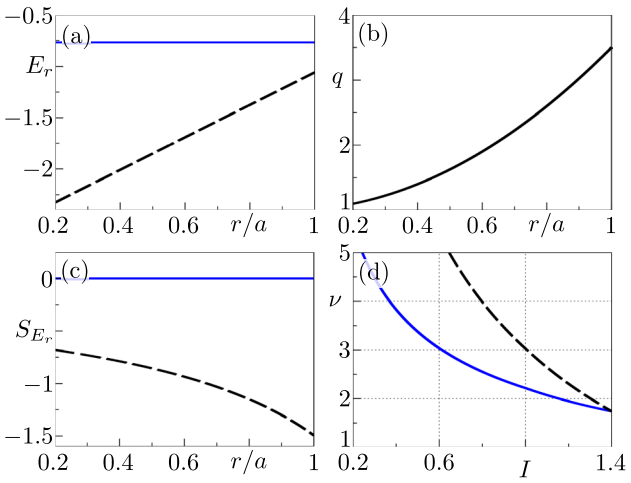

Fig. 2 Radial profiles for the **a** equilibrium electric field, $E_r(r)$, **b** safety factor, $q(r)$, **c** electric field shear, $S_{E_r}(r)$ and **d** unperturbed Hamiltonian frequency, $\nu(I)$. The solid blue line corresponds to the case $E_r(r) =$ constant and the dashed black line to the linear $E_r(r)$ case

not null, this is not enough to make a shearless curve appear, as $|\partial\omega(I)/\partial I| > 0$ for $I \leq (b/a)^2$. However, the effect of a sheared profile is significant due to its changes in the resonance conditions, as we can see from Fig. 2(d). This has a direct influence on chaotic transport, as we will see below.

Let us take the resonant modes $n = 2, 3$ and 4, and consider for their amplitudes $\phi_2 = 2.95 \times 10^{-3}$, $\phi_3 = 3.66 \times 10^{-3}$ and $\phi_4 = 2.08 \times 10^{-3}$. By doing this, we can obtain the Poincaré sections for the perturbed Hamiltonian of both cases, the constant and the linear one, and compare which one is better for the chaotic transport in plasma.

In Fig. 3, we present the Poincaré sections for the monotonic cases of $E_r(r)$. When $S_{E_r}(r)$ is null across the plasma, it can be seen that the chaotic behavior dominates in phase space over the regular one. Most of the trajectories can cross the plasma edge, at $I = 1.00$, indicating an unsatisfactory electric field configuration for confinement. On the other hand, a sheared E_r profile suppresses the chaotic behavior

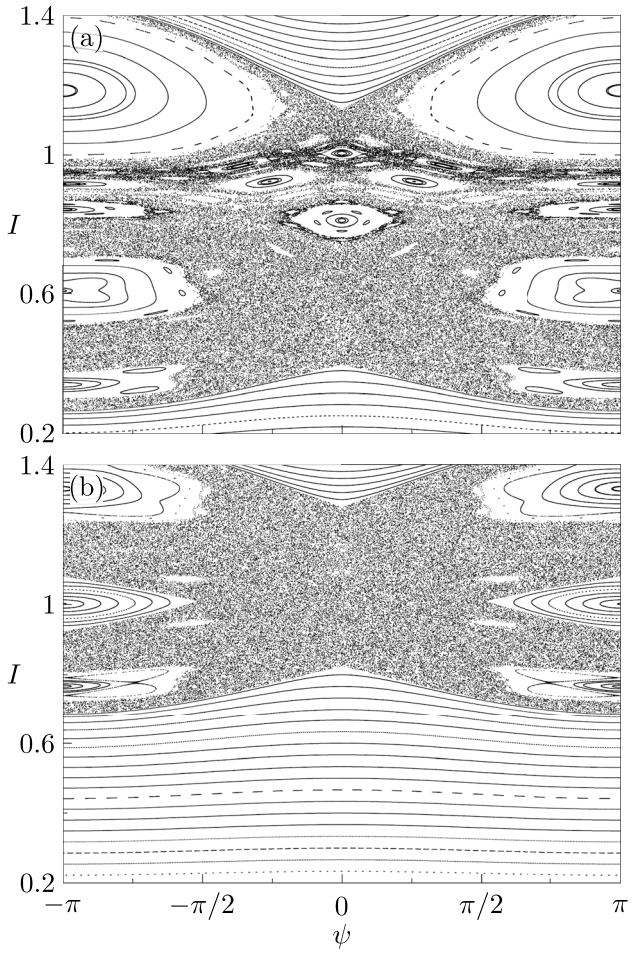

Fig. 3 Poincaré sections for the **a** constant and **b** linear cases of the equilibrium electric field profile. Chaos suppression occurs when we include a sheared profile for $E_r(r)$

and instead establishes more invariant curves. Due to the three resonant modes we are considering, one observes in phase space, for the two scenarios, the formation of three main islands of period-one, with centers at $\psi = \pi$. Their radial positions are associated with the resonance condition profile, $\nu(I) = n$. So, when we adjust the electric field from a constant to a linear one, these islands shift their centers and thereby they change the chaotic dynamics.

Thus, the results indicate that the E_r-shear can reduce the radial chaotic transport in tokamak plasmas, which translates into an improvement of the confinement. Nevertheless, we will show below that there are even better scenarios for achieving this purpose.

3.1.2 Nonmonotonic Electric Field

For now, we indicated that sheared electric field profiles decrease the radial transport in plasmas by suppressing chaotic orbits. However, reversed shear profiles also reduce radial transport and lead to the appearance of robust shearless transport barriers which are more resistant to perturbations than the invariant curves shown in the previous cases [19, 25].

In order to investigate the influence of $E_r(r)$ for the nonmonotonic scenarios, let us vary only the parameters α and β of Eq. (16), keeping the same value of γ used for the linear electric field case, $\gamma = -2.64$. Then, let us keep the same safety factor radial profile, given by (15), parallel velocity, and fluctuating potential parameters as the ones already used.

The maximum value of E_r is constrained to $E_{\max} = -0.77$, which is the same value of γ for the constant electric field case. By doing this, we can modify α and β at the same time, restraining the shearless position of the profile to some value $k = r_s/a = -\beta/(3\alpha)$, where $(\mathrm{d}E_r/\mathrm{d}r)|_{r_s} = 0$.

We analyzed two different values of $I_s = k^2$, 0.53 and 0.60, for which we present their $E_r(r)$, $S_{E_r}(r)$ and $\nu(I)$ profiles in Fig. 4. In panels (a) and (b), we show that both profiles have a shearless point and, therefore, they are shear-reversed. This implies a nonmonotonic frequency profile $\nu(I)$, see panel (c) of the figure, and consequently a violation of the twist condition (14). On using these profiles, we can expect a shearless transport barrier to appear at I_{STB}, for the unperturbed Hamiltonian, where $|\partial\nu(I)/\partial I|_{I_{\mathrm{STB}}} = 0$. Meanwhile, for the perturbed system, the appearance of the shearless barrier depends on the values of ϕ_n, as other works have shown [20, 21]. Also, note that now $n = 2$ is nonresonant.

For the perturbed Hamiltonian system, in order to find the shearless curve, when it exists, it is necessary to calculate the rotation number profile, $\Omega(\psi_0, I_0)$. For this, we adopt a method based on a weighted Birkhoff average, which has been demonstrated to be superconvergent for calculating the rotation number of quasiperiodic orbits [35].

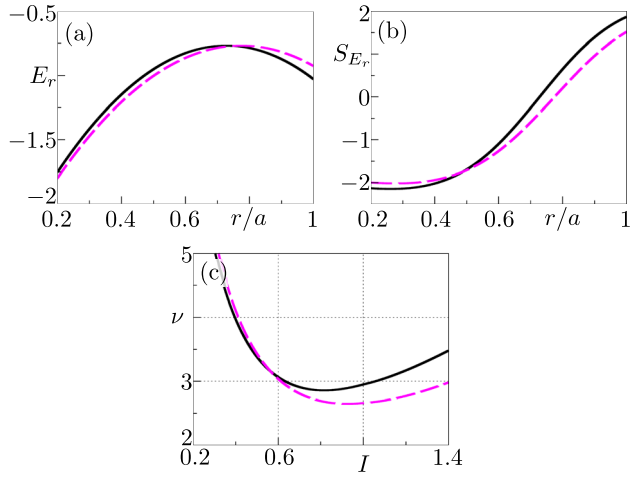

Fig. 4 Radial profiles of **a** the equilibrium electric field, $E_r(r)$, **b** the E_r-shear, $S_{E_r}(r)$, and **c** the unperturbed Hamiltonian frequency, $\nu(I)$. For $I_s = 0.53$ (solid black) and $I_s = 0.60$ (dashed magenta). Note that now $n = 2$ is nonresonant

Basically, one uses a function $g(\tau)$, that converges to zero with infinite smoothness at $\tau(0) = 0$ and $\tau(N) = 1$, with $\tau(j) = j/N$, to weight much less the beginning and the end of the orbit Σ than the terms for which $\tau \sim 0.50$. This function is also called bump. In this work, we consider

$$g(\tau) = \begin{cases} \exp\left(-\dfrac{1}{\tau^p(1-\tau)^p}\right), & \text{for } \tau \in (0,1), \\ 0, & \text{for } \tau \notin (0,1), \end{cases} \tag{18}$$

with $p = 1$, that provides satisfactory results [36, 37]. Other functions can be used, for example, for $p > 1$ or even $g(\tau) = \sin^2(\pi\tau)$; however, the latter one fails to be infinitely smooth at $\tau = 0$ and $\tau = 1$ [36].

The rotation number, Ω, of a regular orbit is independent of the choice of $\mathbf{P}_0$, as long as $\mathbf{P}_0 \in \Sigma$. However, the rotation number radial profile does depend on (ψ_0, I). Different choices of ψ_0 will give different radial profiles, according to the distribution of the orbits on phase space. So, fixing ψ_0, the rotation number radial profile can be calculated as

$$\Omega(\psi_0, I) = \frac{1}{2\pi G_N} \sum_{j=0}^{N-1} g(\tau(j))(\psi_{j+1} - \psi_j), \tag{19a}$$

$$G_N = \sum_{j=0}^{N} g(\tau(j)). \tag{19b}$$

Note that for $g(\tau) = 1$ the equation above returns to the usual definition of rotation number [28]; however, the convergence is slower because assumes equal weights at any time of the orbit.

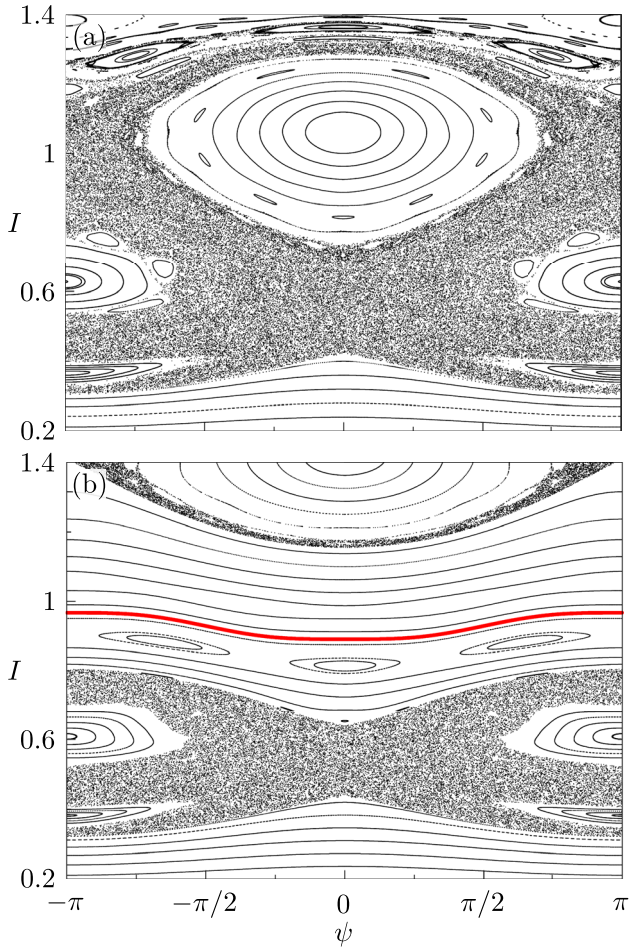

Fig. 5 Poincaré sections for **a** $I_s = 0.53$ and **b** $I_s = 0.60$. A shearless curve is highlighted in red

From Fig. 5, we see that, when $I_s = 0.53$, no resistance to the chaotic transport appears, most of the orbits escape outside the plasma. Nonetheless, by modifying the electric field, by taking $I_s = 0.60$, a great suppressing of the chaotic transport occurs and, moreover, a shearless curve can be found close to the plasma edge, so confining most of the trajectories. The associated shearless curve was identified through the rotation number profile shown in Fig. 6(b), estimating the value I_{STB} for which $\left(\partial\Omega(\psi_0, I)/\partial I\right)_{I_{\text{STB}}} = 0$. The initial condition $\mathbf{P}_{\text{STB}} = (\psi_0, I_{\text{STB}})$ generates in phase space the invariant torus related to the barrier.

Note that the $\Omega(\psi_0, I)$ profile for the linear $E_r(r)$ case does not have any shearless point, i.e., it has no shearless curve, panel (a) of the figure. As we explained before, the twist condition is not broken anywhere for that system. In fact, for both the linear and the parabolic $E_r(r)$, rotation number profiles deviate just a little from the frequency profiles of the unperturbed Hamiltonian former cases.

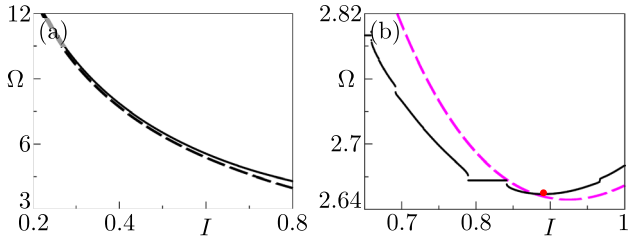

Fig. 6 Rotation number profiles for **a** the unperturbed (dashed) and perturbed (solid) Hamiltonians associated with the linear radial electric field scenario, and rotation number profiles for **b** the unperturbed (dashed magenta) and perturbed (black) Hamiltonians associated with the nonmonotonic radial electric field

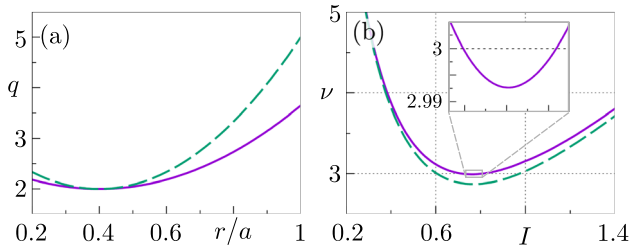

Fig. 7 **a** Nonmonotonic safety factor profile and **b** corresponding resonance condition for $q_a = 3.65$ (solid purple) and $q_a = 5.00$ (dashed green)

3.2 Nonmonotonic Magnetic Field

Besides the influence of the radial electric field profile, the equilibrium magnetic field profile can also change the transport in Horton's model. In the previous subsection, we applied a monotonic safety factor profile, together with a monotonic and a nonmonotonic electric field profile, Figs. 2 and 4. The nonmonotonic configuration results in the onset of a shearless curve in phase space, which can be broken up by the variation of the electric field profile, Fig. 5. In this section, we will show that by modifying the safety factor with a nonmonotonic profile, the frequency profile of the system is changed and, consequently, its transport.

The nonmonotonic safety factor profile used in this paper is given by

$$q(r) = q_{\rm m} + q''_{\rm m}(r - r_{\rm m})^2, \tag{20}$$

where

$$q''_{\rm m}(q_a) = \frac{q_a - q_{\rm m}}{(1 - r_{\rm m})^2}, \tag{21}$$

and $r_{\rm m}$ is the radial location of the safety factor profile minimum, $q_{\rm m} = q(r_{\rm m})$. The safety factor at the plasma edge, q_a, is the control parameter chosen to analyze the influence of the magnetic field profile. It is related to the plasma current, an easily obtained experimental measure [38].

We choose two values of the safety factor at the plasma edge to analyze the Poincaré section, $q_a = 5.00$ and $q_a = 3.65$. The corresponding $q(r)$ and frequency profiles are shown in Fig. 7. The other profile parameters are fixed at $r_{\rm m} = 0.40$ and $q_{\rm m} = 2.00$. For the electric field radial profile we use $I_{\rm s} = 0.5$.

The same resonant modes, $n = 3$ and 4 are found in both nonmonotonic safety factor configurations. They also have a shearless point at $I_{\rm STB} \approx 0.8$. For $q_a = 3.65$, the two resonances associated with $n = 3$ are close to each other, as seen in the inset of Fig. 7(b).

Figure 8 shows the Poincaré sections for $q_a = 5.00$ and $q_a = 3.65$. In the first one, the configuration of orbits indicates a large transport: the chaotic orbits spread in a large portion of phase space, crossing the plasma edge, at $I = 1.00$, Fig. 7(a). The larger islands are associated with the

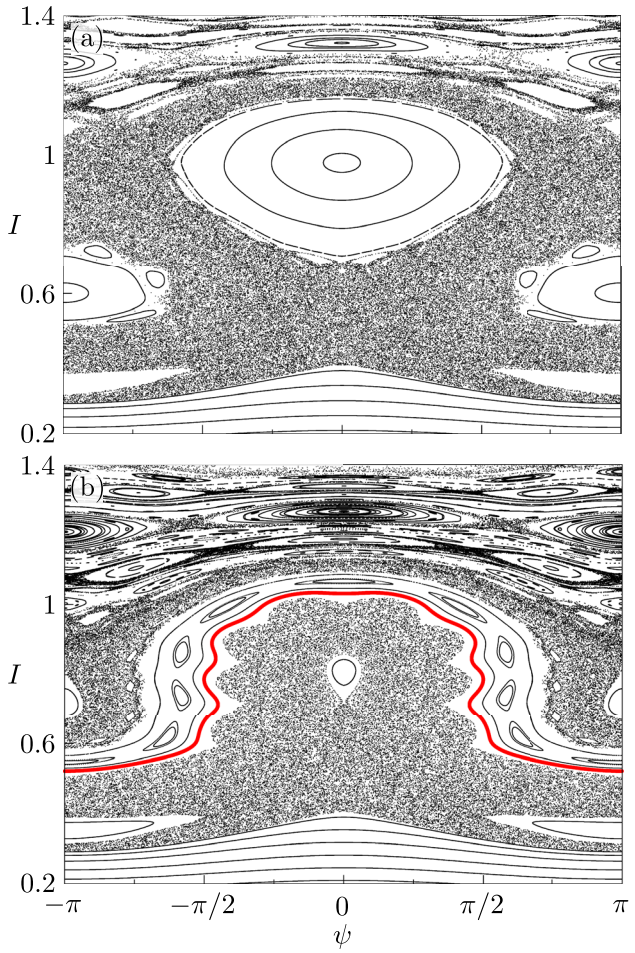

Fig. 8 Poincaré section using nonmonotonic safety factor profile for **a** $q_a = 5.0$ and **b** $q_a = 3.65$. The shearless invariant curve (red) acts as a robust transport barrier in phase space

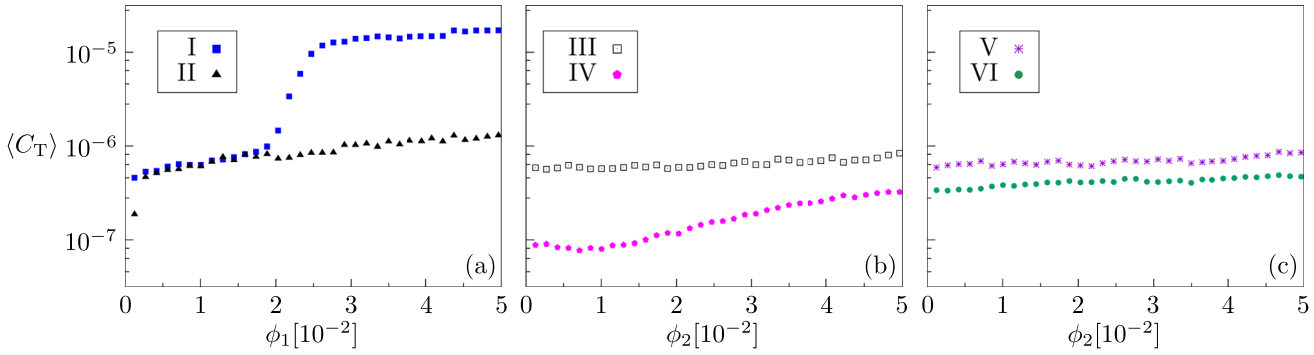

Fig. 9 **a** E_r constant (filled blue squares) and E_r linear (filled black triangles). **b** $I_s = 0.53$ (empty black squares) and $I_s = 0.60$ (filled magenta pentagons). **c** $q_a = 5.00$ (filled green circles) and $q_a = 3.65$ (purple crosses)

resonant mode $n = 3$, localized at $I \approx 0.6$ and $I \approx 1.0$, Fig. 7. The same islands are present for $q_a = 3.65$, although their radial locations are close to I_{STB}, Fig. 7(b). For this q_a value, the phase space presents a shearless curve, marked in red, that acts as a transport barrier, preventing internal chaotic orbits to be transported across the plasma edge.

In summary, the nonmonotonic safety factor changes the frequency profile of the system, and consequently, its resonance conditions. The results in this subsection indicate a relation between the safety factor profile with the onset and breakup of the shearless curve, which is a barrier to transport in phase space. In the next section, we will show that the presence of a shearless curve in phase space systematically reduces the transport coefficient of the system, even when the fluctuating amplitude modes are increased.

4 Transport Coefficient Analysis

In this section, we analyze the chaotic transport dependence on the amplitude of the fluctuating modes ϕ_n for each one of the plasma profile configurations used in Figs. 3, 5 and 8. Those profiles are categorized into six cases, as shown in Table 1.

To quantify this transport, we calculate the transport coefficient $\langle C_T \rangle$, which is the average of the running transport coefficient $C_T(t)$, a quantification of the radial transport in phase space. More precisely, given an ensemble of $\mathcal{N}$ orbits, the running transport coefficient is proportional to the mean squared deviation of the action variables $I(t)$ with respect to the initial conditions $I(0)$; it is given by

$$C_T(t) = \frac{1}{2t\mathcal{N}} \sum_{\ell=1}^{\mathcal{N}} \left[I^{(\ell)}(t) - I^{(\ell)}(0) \right]^2, \tag{22}$$

where $I^{(\ell)}(t)$ is the action of the ℓ-th particle of the ensemble, at the time t. The mean transport coefficient is given by the time average of $C_T(t)$, i.e.,

$$\langle C_T \rangle = \frac{1}{t_{\text{f}} - t_{\text{i}}} \sum_{t_j = t_{\text{i}}}^{t_{\text{f}}} (C_T(t_j)) \tag{23}$$

where t_{i} is the time at which the convergence of $C_T(t)$ is observed to set in.

In the ensemble, some orbits will be chaotic, but others are regular (invariant curves or islands). The chaotic orbits will contribute to increasing $\langle C_T \rangle$, and the regular ones tend to decrease it. As the coefficient is an average over a large ensemble, higher values of $\langle C_T \rangle$ indicate large portions of chaotic orbits in the phase space, which have a large transport in the action coordinate. On the other hand, small values of $\langle C_T \rangle$ indicate a small portion of chaotic orbits in phase space, which have a small transport in action coordinate. For numerical purposes, we computed the running transport coefficient for an ensemble of $\mathcal{N} = 10^3$ ramdonly chosen orbits, with action initial conditions chosen such that $I^{(\ell)}(0) \in [0.2, 1]$, which were integrated until $t_{\text{f}} = (2\pi/\omega_0) \times 10^5$, with a transient of $t_{\text{i}} = 0.3\, t_{\text{f}}$.

We computed the transport coefficient $\langle C_T \rangle$ varying the amplitude of the higher associated nonresonant mode, which means, for the configurations of Fig. 2 (Cases I and II), the nonresonant mode $n = 1$, and for the plasma profiles of Figs. 4 (Cases III and IV) and 7 (Cases V and VI), the nonresonant mode $n = 2$. The associated nonresonant modes

Table 1 Plasma configurations for the equilibrium electric and magnetic fields radial profiles considered in this article

Case	E_r profile	q profile
I	constant	monoto
II	linear	monot
III	nonmonot. $k = 0.53$	monot
IV	nonmonot. $k = 0.60$	monot
V	nonmonot. $k = 0.50$	nonmonot. $q_a = 5.00$
VI	nonmonot. $k = 0.50$	nonmonot. $q_a = 3.65$

amplitudes were varied from 0 to 5×10^{-2}, and the obtained results are presented in Fig. 9.

Both configurations with monotonic radial electric fields have the higher transport coefficient values among all the configurations considered. The results in Fig. 9(a) indicate a similar transport coefficient until $\phi_1 \approx 2 \times 10^{-2}$, and for higher values, the transport for Case I is substantially higher than for Case II. This result indicates that the radial electric field shear S_{E_r} provides suppression of chaotic orbits in phase space, as identified in Fig. 3.

Applying nonmonotonic radial electric field profiles, we can reduce the transport coefficient in comparison with the monotonic profiles scenarios, Fig. 9(b). Considering Cases III and IV, we found that the latter has a smaller coefficient, therefore, the shearless curve presented in Fig. 5(b) provides a robust barrier to the transport in phase space. Futhermore, the transport coefficient of Case III is similar to Case II, indicating that the shearless curve is not present in the phase space of III, for any value of ϕ_2.

Finally, the influence of the safety factor profile in the transport coefficient is presented in Fig. 9(c). For Case V, in comparison to Case III, the addition of a nonmonotonic q profile does not change the transport coefficient. However, for Case VI, the transport coefficient is reduced, due to the presence of the shearless curve in phase space, Fig. 8(b). In summary, the nonmonotonic safety factor profile can reduce the transport in phase space, and its profile influences the onset and breakup of the shearless curve.

5 Conclusions

In this work, we applied a transport model to describe the trajectory of test particles at the tokamak plasma edge subject to the $\mathbf{E} \times \mathbf{B}$ drift motion, associated with anomalous transport. Numerical simulations of the corresponding Hamiltonian system were done to obtain the trajectory of the test particle, plotted at a Poincaré section. Those orbits can be regular or chaotic, associated with particle transport.

We considered different configurations of plasma electric and magnetic field profiles. Two monotonic electric field profiles were considered, a constant and a linear one. The Poincaré sections obtained indicate low confinement of orbits for the constant electric field configuration. In addition, the linear profile, which has an electric shear, presented a suppression of the chaotic orbits.

Considering nonmonotonic electric field profiles, with reversed shear, chaos suppression is also present. Moreover, in such systems with nonmonotonic profiles, the phase space can present a shearless curve, that acts as a robust transport barrier in phase space, preventing the chaotic orbits from leaving the plasma. However, this transport barrier can be broken up by varying the plasma equilibrium electric field profile.

In the last plasma configuration, both the electric and magnetic field profiles were considered nonmonotonic. This configuration also presented the shearless transport barrier. Nonetheless, the results obtained indicate that, by variations in the safety factor profiles, the shearless curve could also be broken up.

Finally, we made an analysis of the transport coefficient in each plasma configuration presented in this paper. The transport coefficient was numerically obtained by calculating the squared mean deviation of the particles orbits, as a function of a perturbation mode amplitude. The results indicate low confinement for a constant electric field. The addition of sheared electric field profiles, such as in the linear or parabolic cases, reduced the transport coefficients. On introducing nonmonotonic profiles of the electric and magnetic fields, shearless transport barriers appear which reduce even more the radial transport coefficient.

In summary, the results in this paper indicate that by using Horton's model to study the anomalous transport of particles at the plasma edge, sheared plasma profiles tend to reduce the plasma transport, as predicted by the $\mathbf{E} \times \mathbf{B}$ shear stabilization models. They predict a reduction in transport where the electric shear is high. Nevertheless, the effect of shearless transport barriers, associated with regions of null shear, present in nonmonotonic profiles, reduces the transport.

Appendix. Normalization of the Model Equations

In this appendix, we outline the normalization of the variables and parameters of the Hamiltonian system used in this paper. The characteristic scales of the system are chosen as $a_c = a$ (length), $E_c = |E_r(r = a)|$ (electric field) and $B_0 = B_c$ (magnetic field). That is, the normalized quantities, denoted with a prime, are

$$a' = \frac{a}{a_c},\ E'_r = \frac{E_r}{E_c},\ B' = \frac{B}{B_c}. \tag{24}$$

The remaining parameters are chosen according to

$$\phi'_n = \frac{\phi_n}{aE_c},\ \ v'_{\parallel} = \frac{B_c}{E_c} v_{\parallel} \tag{25a}$$

$$t' = \frac{E_c}{aB_c} t,\ \ \omega'_0 = \frac{a_c B_c}{E_c} \omega_0. \tag{25b}$$

Finally, the numerical values of the parameters are: $\omega_0 = 5.7, v_{\parallel} = 2.0$, and $(\phi_2, \phi_3, \phi_4) = (1.95, 3.66, 2.08) \times 10^{-3}$.

Acknowledgements The Centre de Calcul Intensif d'Aix-Marseille is acknowledged for granting access to its high performance computing resources. L.A. Osorio-Quiroga thanks Cristel Chandre for advising him on the rotation number calculation.

Funding The authors received financial support from the Brazilian Federal Agencies (CNPq), grants 304616/2021-4 and 302665/2017-0, the São Paulo Research Foundation (FAPESP, Brazil) under grants 2018/03211-6, 2020/01399-8, 2022/04251-7, 2022/08699-2 and 2022/05667-2, the Coordenação de Aperfeiçoamento de Pessoal de Nível Superior (CAPES) under Grant No. 88881.143103/2017-01, and the Comité Français d'Evaluation de la Coopération Universitaire et Scientifique avec le Brésil (COFECUB) under Grant No. 40273QA-Ph908/18.

Declarations

Competing Interests The authors declare no competing interests.

References

1. S.C. Cowley, The quest for fusion power. Nat. Phys. **12**(5), 384 (2016)
2. W. Horton, *Turbulent transport in magnetized plasmas* (World Scientific, Singapore, 2018)
3. R. Wolf, Internal transport barriers in tokamak plasmas. Plasma Phys. Controlled Fusion **45**(1), 1 (2002)
4. M. Cavedon, T. Pütterich, E. Viezzer, G. Birkenmeier, T. Happel, F. Laggner, P. Manz, F. Ryter, U. Stroth, ASDEX Upgrade Team, et al., Interplay between turbulence, neoclassical and zonal flows during the transition from low to high confinement mode at ASDEX upgrade. Nucl. Fusion **57**(1), 014002 (2016)
5. K.H. Burrell, Effects of E × B velocity shear and magnetic shear on turbulence and transport in magnetic confinement devices. Phys. Plasmas **4**, 1499 (1997)
6. J.W. Connor, T. Fukuda, X. Garbet, C. Gormezano, V. Mukhovatov, M. Wakatani, A review of internal transport barrier physics for steady-state operation of tokamaks. Nucl. Fusion **44**, 1 (2004)
7. X. Garbet, P. Mantica, C. Angioni, E. Asp, Y. Baranov, C. Bourdelle, R. Budny, F. Crisanti, G. Cordey, L. Garzotti et al., Physics of transport in tokamaks. Plasma Phys. Controlled Fusion **46**(12B), 557 (2004)
8. R. Moyer, K. Burrell, T. Carlstrom, S. Coda, R. Conn, E. Doyle, P. Gohil, R. Groebner, J. Kim, R. Lehmer et al., Beyond paradigm: Turbulence, transport, and the origin of the radial electric field in low to high confinement mode transitions in the DIII-D tokamak. Phys. Plasmas **2**(6), 2397 (1995)
9. T. Kobayashi, K. Itoh, T. Ido, K. Kamiya, S.-I. Itoh, Y. Miura, Y. Nagashima, A. Fujisawa, S. Inagaki, K. Ida, Turbulent transport reduction induced by transition on radial electric field shear and curvature through amplitude and cross-phase in torus plasma. Sci. Rep. **7**(1), 14971 (2017)
10. K. Kamiya, K. Itoh, S.-I. Itoh, Experimental validation of non-uniformity effect of the radial electric field on the edge transport barrier formation in JT-60U H-mode plasmas. Sci. Rep. **6**(1), 30585 (2016)
11. I.L. Caldas, R.L. Viana, C.V. Abud, J.C.D.D. Fonseca, Z.D.O. Guimarães Filho, T. Kroetz, F.A. Marcus, A.B. Schelin, J. Szezech, D.L. Toufen, et al., Shearless transport barriers in magnetically confined plasmas. Plasma Phys. Control. Fusion **54**, 124035 (2012)
12. W. Horton, Onset of stochasticity and the diffusion approximation in drift waves. Plasma Phys. Control. Fusion **27**, 937 (1985)
13. G.A. Oda, I.L. Caldas, Dimerized island chains in tokamaks. Chaos Solitons & Fractals **5**(1), 15 (1995)
14. R. Egydio de Carvalho, A.M. Ozorio de Almeida, Integrable approximation to the overlap of resonances. Phys. Lett. A **162**(6), 457–463 (1992)
15. G. Corso, F.B. Rizzato, Manifold reconnection in chaotic regimes. Phys. Rev. E **58**(6), 8013 (1998)
16. D. del-Castillo-Negrete, Chaotic transport in zonal flows in analogous geophysical and plasma systems. Phys. Plasmas **7**, 1702 (2000)
17. P.J. Morrison, Magnetic field lines, hamiltonian dynamics, and nontwist systems. Phys. Plasmas **7**, 2279 (2000)
18. W. Horton, H.B. Park, J.M. Kwon, D. Strozzi, P.J. Morrison, D.I. Choi, Drift wave test particle transport in reversed shear profile. Phys. Plasmas **5**, 3910 (1998)
19. K.C. Rosalem, M. Roberto, I.L. Caldas, Influence of the electric and magnetic shears on tokamak transport. Nucl. Fusion **54**, 064001 (2014)
20. F.A. Marcus, M. Roberto, I.L. Caldas, K.C. Rosalem, Y. Elskens, Influence of the radial electric field on the shearless transport barriers in Tokamaks. Phys. Plasmas **26**, 022302 (2019)
21. L. Osorio, M. Roberto, I.L. Caldas, R.L. Viana, Y. Elskens, Onset of internal transport barriers in tokamaks. Phys. Plasmas **28**, 082305 (2021)
22. M. El Mouden, D. Saifaoui, B. Zine, M. Eddahoy, Transport barriers with magnetic shear in a tokamak. J. Plasma Phys. **73**, 439 (2007)
23. G. Grime, M. Roberto, R. Viana, Y. Elskens, I. Caldas, Shearless bifurcations in particle transport for reversed-shear Tokamaks. J. Plasma Phys. **89**(1), 835890101 (2023)
24. C.P. Ritz, R.D. Bengtson, S. Levinson, E. Powers, Turbulent structure in the edge plasma of the TEXT tokamak. Phys. Fluids **27**(12), 2956–2959 (1984)
25. J.-M. Kwon, W. Horton, P. Zhu, P.J. Morrison, H.-B. Park, D.I. Choi, Global drift wave map test particle simulations. Phys. Plasmas **7**, 1169 (2000)
26. A.J. Lichtenberg, M.A. Lieberman, *Regular and chaotic motion* (Springer Verlag, New York, 1997)
27. J.M. Greene, A method for determining a stochastic transition. J. Math. Phys. **20**(6), 1183 (1979)
28. J.D. Meiss, Symplectic maps, variational principles, and transport. Rev. Mod. Phys. **64**, 795 (1992)
29. R. Viana, I.L. Caldas, J. Szezech Jr., A. Batista, C. Abud, A. Schelin, M. Mugnaine, M. Santos, B. Leal, B. Bartoloni et al., Transport barriers in symplectic maps. Braz. J. Phys. **51**, 899 (2021)
30. J.D. Szezech Jr., I.L. Caldas, S.R. Lopes, R.L. Viana, P.J. Morrison, Transport properties in nontwist area-preserving maps. Chaos **19**, 043108 (2009)
31. P.J. Prince, J.R. Dormand, High order embedded Runge-Kutta formulae. J. Comput. Appl. Math. **7**(1), 67 (1981)
32. I.C. Nascimento, Y.K. Kuznetsov, J.H.F. Severo, A.M.M. Fonseca, A. Elfimov, V. Bellintani, M. Machida, M.V.A.P. Heller, R.M.O. Galvão, E.K. Sanada, Plasma confinement using biased electrode in the TCABR tokamak. Nucl. Fusion **45**, 796 (2005)
33. F.A. Marcus, I.L. Caldas, Z.O. Guimarães-Filho, P.J. Morrison, W. Horton, Y.K. Kuznetsov, I.C. Nascimento, Reduction of chaotic particle transport driven by drift waves in sheared flows. Phys. Plasmas **15**(11), 112304 (2008)
34. J.H.F. Severo, G.P. Canal, G. Ronchi, N.B. Andrade, T. Fernandes, M.Y. Ikeda, M.P. Collares, R.M.O. Galvão, I.C. Nascimento, M. Tendler, Overview of plasma rotation studies on the TCABR tokamak. Plasma Phys. Controlled Fusion **63**(7), 075001 (2021)
35. S. Das, J.A. Yorke, Super convergence of ergodic averages for quasiperiodic orbits. Nonlinearity **31**(2), 491 (2018)
36. S. Das, Y. Saiki, E. Sander, J.A. Yorke, Quantitative quasiperiodicity. Nonlinearity **30**(11), 4111 (2017)
37. E. Sander, J. Meiss, Birkhoff averages and rotational invariant circles for area-preserving maps. Physica D **411**, 132569 (2020)

38. J. Wesson, D.J. Campbell, *Tokamaks* (Oxford University Press, New York, 2011)